



# Optical response of noble metal nanostructures: quantum surface effects in crystallographic facets

A. RODRÍGUEZ ECHARRI,<sup>1,2</sup> P. A. D. GONÇALVES,<sup>2</sup> C. TSERKEZIS,<sup>2</sup>   
 F. JAVIER GARCÍA DE ABAJO,<sup>1,3</sup> N. ASGER MORTENSEN,<sup>2,4</sup> AND JOEL D. COX<sup>2,4,\*</sup>

<sup>1</sup>ICFO—Institut de Ciències Fotoniques, The Barcelona Institute of Science and Technology, 08860 Castelldefels (Barcelona), Spain

<sup>2</sup>Center for Nano Optics, University of Southern Denmark, Campusvej 55, DK-5230 Odense M, Denmark

<sup>3</sup>ICREA—Institut Català de Recerca i Estudis Avançats, Passeig Lluís Companys 23, 08010 Barcelona, Spain

<sup>4</sup>Danish Institute for Advanced Study, University of Southern Denmark, Campusvej 55, DK-5230 Odense M, Denmark

\*Corresponding author: cox@mci.sdu.dk

Received 12 October 2020; revised 8 February 2021; accepted 29 March 2021 (Doc. ID 412122); published 17 May 2021

Noble metal nanostructures are ubiquitous elements in nano-optics, supporting plasmon modes that can focus light down to length scales commensurate with nonlocal effects arising from quantum confinement and spatial dispersion in the underlying electron gas. Quantum and nonlocal effects can be more prominent in crystalline noble metals, due to their lower intrinsic loss (when compared with their polycrystalline counterparts), and because particular crystal facets give rise to distinct electronic surface states whose signatures can be imprinted in the optical response of a structure. Here, we employ an atomistic method to describe nonclassical effects impacting the optical response of crystalline noble metal surfaces and demonstrate that these effects can be well captured using a set of surface-response functions known as Feibelman  $d$ -parameters determined from such quantum-mechanical models. In particular, we characterize the  $d$ -parameters associated with the (111) and (100) crystal facets of gold, silver, and copper, emphasizing the importance of quantum surface effects associated with electron wave function spill-out/spill-in and with the surface-projected band gap emerging from the atomic-layer corrugation. Furthermore, we show that the extracted  $d$ -parameters can be straightforwardly applied to describe the optical response of various nanoscale metal morphologies of interest, including metallic ultrathin films, graphene–metal heterostructures hosting ultraconfined acoustic graphene plasmons, and crystallographic faceted metallic nanoparticles supporting localized surface plasmons. We envision that the  $d$ -parameters presented here, along with the prescription to extract and apply them, could help circumvent computationally expensive first-principles atomistic calculations to describe quantum nonlocal effects in the optical response of mesoscopic crystalline metal surfaces, which are becoming widely available with increasing control over morphology down to atomic length scales for state-of-the-art experiments in nano-optics. © 2021 Optical Society of America under the terms of the OSA

Open Access Publishing Agreement

<https://doi.org/10.1364/OPTICA.412122>

## 1. INTRODUCTION

Metals support collective oscillations of their conduction electrons, known as plasmons, with light-trapping and light-manipulation capabilities at nanometer length scales (i.e., well below the diffraction limit imposed by traditional optics [1,2]). The wealth of fundamental explorations in plasmonics over the last couple of decades has contributed to shape the field of nano-optics [3,4], holding great promises for nanophotonic-based technologies including theranostics [5,6], photocatalysis [7,8], structural coloring [9], solar energy harvesting [10,11], and quantum information [12–14]. Advances in modern nanofabrication techniques have fueled plasmonics research further by enabling the realization of nano-optical devices operating at deeply subwavelength scales [15,16]. As current state-of-the-art capabilities can pattern metallic nanostructures down to the few-nanometer regime [17–19]—where the frontiers of quantum and classical physics

coalesce—new routes towards next-generation plasmon-based technologies begin to emerge, while also posing new challenges in understanding and modeling their optical response at truly nanometric scales [14,20,21].

The realization of thin crystalline noble metal films [22–25] is key to cutting-edge explorations of novel plasmonic devices: metallic nanostructures with a high degree of crystallinity are anticipated to exhibit lower Ohmic losses when compared to their polycrystalline kins [26], with the recent observation of plasmons in laterally patterned few-atom-thick crystalline silver films partially confirming this intuition [19]. Furthermore, it is well established in surface science that (111) noble metal surfaces possess Shockley surface states (SSs), with features resembling those of a two-dimensional electron gas (2DEG) [27–29]. The 2D-like plasmon modes supported by Shockley SSs [29,30] can be characterized, for example, by angle-resolved spectroscopy

[31–33], and play a role in near-field light–matter interactions at such surfaces.

While *ab initio* methods capture nonclassical effects in the optical response of ultrathin metal films or few-atom metal clusters [34,35], they often require substantial computational efforts that rapidly become unfeasible for structures with characteristic sizes  $\gtrsim 10$  nm; nevertheless, precision within  $\sim 10$  nm is what is currently afforded by state-of-the-art top-down nanofabrication techniques. One of the overarching challenges in theoretical nano-optics is thus to describe the optical properties of nanostructured metals by solving Maxwell’s equations while accounting for—in the response functions entering the constitutive relations—quantum-mechanical effects that emerge when electrons are confined in low-dimensional systems, ideally without resorting to demanding numerical approaches that provide limited insights into the underlying physics. Fortunately, the situation is somewhat simplified in metals by their ability to effectively screen electromagnetic fields, which leads to an optical response dominated by surface effects. In this context, the concept of microscopic surface-response functions, such as the Feibelman  $d$ -parameters [21,36–40], offers a practical and scalable recipe to simultaneously incorporate quantum-mechanical phenomena, such as electronic spill-out, nonlocality, and surface-enabled Landau damping, into the optical response of metal nanostructures [21,36–38,41], as has been recently demonstrated experimentally [42].

Here, we apply a quantum-mechanical framework employing a one-dimensional (1D) potential that describes a vertical stack of (homogeneous) atomic layers [43], to model crystalline metals. The wave functions obtained by solving the corresponding Schrödinger equation are then used to compute the nonlocal optical response of selected noble metal (gold, silver, and copper) films with specific crystallographic orientations—namely, the (100) and (111) surfaces—from which we extract the associated Feibelman  $d$ -parameters. We demonstrate that the  $d$ -parameters obtained for a thick film (tantamount to a semi-infinite metal), once tabulated (as we do here), can be straightforwardly incorporated into a wide range of electromagnetic problems, ranging from analytical solutions for simple geometries [21,37,38] to full-wave numerical electromagnetic solvers of realistic particles [42], to accurately describe quantum-mechanical effects impacting the optical response of the system [38,42]. We anticipate that the results presented herein could be widely deployed to describe ongoing experiments and engineer future nanoscale plasmonic devices at the extreme nanoscale.

## 2. RESULTS AND DISCUSSION

In classical electrodynamics, a metal surface is commonly described by a step-like dielectric function that changes abruptly from the bulk, local dielectric function of the metal,  $\epsilon_m \equiv \epsilon_m(\omega)$ , to that of the adjacent dielectric,  $\epsilon_d \equiv \epsilon_d(\omega)$ . However, this rudimentary prescription can be augmented with  $d$ -parameter-corrected boundary conditions that incorporate quantum effects associated with the optical response of metal surfaces to leading order. Specifically, for a  $p$ -polarized electromagnetic field impinging on a metal surface from the dielectric side, the nonretarded reflection and transmission coefficients read [21,37–39]

$$r_{\text{dm}} = \frac{\epsilon_m - \epsilon_d + (\epsilon_m - \epsilon_d) Q(d_{\perp} + d_{\parallel})}{\epsilon_m + \epsilon_d - (\epsilon_m - \epsilon_d) Q(d_{\perp} - d_{\parallel})}, \quad (1a)$$

$$t_{\text{dm}} = \frac{2\epsilon_d}{\epsilon_m + \epsilon_d - (\epsilon_m - \epsilon_d) Q(d_{\perp} - d_{\parallel})}, \quad (1b)$$

respectively. Here,  $Q$  is the in-plane wave vector (i.e., parallel to the interface), while  $d_{\perp} \equiv d_{\perp}(\omega)$  and  $d_{\parallel} \equiv d_{\parallel}(\omega)$  denote the frequency-dependent, complex-valued quantum surface-response functions introduced by Feibelman [21,36–38] (see Appendix A). In addition, for  $p$ -polarized light impinging on the interface from the metal side, the corresponding nonretarded reflection and transmission coefficients read

$$r_{\text{md}} = \frac{\epsilon_d - \epsilon_m + (\epsilon_m - \epsilon_d) Q(d_{\perp} + d_{\parallel})}{\epsilon_m + \epsilon_d - (\epsilon_m - \epsilon_d) Q(d_{\perp} - d_{\parallel})}, \quad (2a)$$

$$t_{\text{md}} = \frac{2\epsilon_m}{\epsilon_m + \epsilon_d - (\epsilon_m - \epsilon_d) Q(d_{\perp} - d_{\parallel})}. \quad (2b)$$

Note that, in general,  $r_{\text{md}} \neq -r_{\text{dm}}$  for  $d_{\alpha} \neq 0$ , where  $\alpha \in \{\perp, \parallel\}$ . Equipped with Eqs. (1) and (2), the overall Fabry–Perot (FP)-like reflection coefficient of the composite dielectric–metal–dielectric heterostructure can be determined via

$$R = r_{\text{dm}} + \frac{t_{\text{dm}} t_{\text{md}} r_{\text{md}} e^{-2QL}}{1 - r_{\text{md}} r_{\text{dm}} e^{-2QL}}, \quad (3)$$

where  $L$  denotes the metal film thickness.

The above quantum-surface-corrected description requires as inputs only the local, frequency-dependent dielectric functions of the metal  $\epsilon_m$  and of the surrounding dielectric  $\epsilon_d$ , along with the frequency-dependent Feibelman  $d$ -parameters ( $d_{\perp}$  and  $d_{\parallel}$ ). For a particular dielectric–metal interface, the  $d$ -parameters can be obtained via first-principles quantum-mechanical methods [e.g., time-dependent density-functional theory (TDDFT)] [39], semiclassical or quantum-informed models [36], or experimentally [40,42].

In what follows, we obtain the  $d$ -parameters from the reflection coefficients associated with crystalline noble metal surfaces by performing nonclassical optical response calculations based on the random-phase approximation (RPA), employing the quantum-mechanical model reported in Ref. [44] (see Appendix A for details). In the RPA formalism applied here, the noninteracting susceptibility is constructed from single-particle wave functions  $\Psi_i(\mathbf{r})$  that satisfy the Schrödinger equation for a 1D phenomenological potential  $V(z)$  characterizing each crystalline metal [43]. To describe *crystalline* metals, we employ the so-called atomic layer potential (ALP), which are simple parametrized potentials that capture the atomic corrugations in the direction perpendicular to the surface, and have been designed to reproduce the salient features of the bulk and semi-infinite surface electronic structures [43]. The ALP-RPA description thus incorporates the effects of electronic band structure, electron spill-in/out, and transverse atomic corrugation in the optical response of layered silver (Ag), gold (Au), and copper (Cu) films with (100) or (111) crystallographic orientation (see Table 3).

Dynamical core-electron screening (i.e., due to low-lying occupied  $d$ -bands), which plays an important role in the optical response of noble metals [45,46], is incorporated in the ALP-RPA model through a polarizable background with dielectric function  $\epsilon_b(\omega)$ . A comprehensive description of the calculation is provided in Appendix A. To maintain fidelity with experimental data, we follow Ref. [47] and construct  $\epsilon_b(\omega)$  by subtracting the free-electron component from the experimentally tabulated dielectric function,

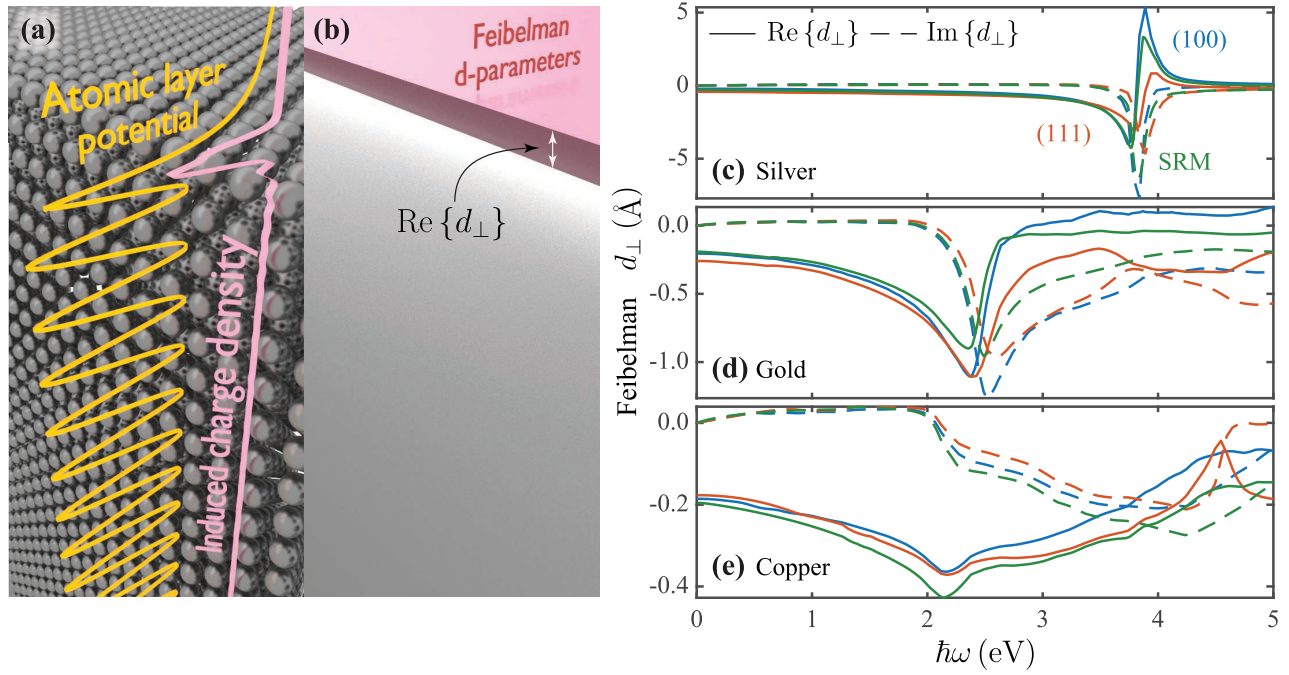


**Fig. 1.** Feibelman  $d$ -parameters for noble metals with distinct crystallographic surfaces. (a) Illustration of a semi-infinite crystalline noble metal surface comprising vertically stacked atomic planes and characterized by a phenomenological atomic layer potential (ALP), for which the optical response is computed in atomistic quantum-mechanical calculations (ALP-RPA); extraction of the Feibelman  $d$ -parameters associated with the metal surface facilitates a mesoscopic, surface-corrected treatment of its optical response, portrayed as the plane in (b) representing the centroid of the induced charge (given by  $\text{Re}\{d_{\perp}\}$ ), which incorporates quantum nonlocal effects encoded in a surface dipole density. (c)–(e) Real (solid curves) and imaginary (dashed curves) parts of  $d_{\perp}$  for the (111) and (100) facets of Ag, Au, and Cu, along with the  $d_{\perp}$  obtained in the specular reflection model (SRM), as indicated by the color-matched legends in panel (c).

**Table 1.** Drude Parameters Characterizing Free-Electron Gas Contributions to Noble Metal Dielectric Functions<sup>a</sup>

Metal	$\hbar\omega_p^{\text{exp}}$ (eV)	$\hbar\gamma^{\text{exp}}$ (meV)
Ag	9.17	21
Au	9.06	71
Cu	8.88	103

<sup>a</sup>Phenomenological parameters used for a Drude-like dielectric function that is compatible with experimental data [48]. The background contribution  $\epsilon_b$  is shown in Fig. 7.

$\epsilon_m^{\text{exp}}$  [48], such that  $\epsilon_b(\omega) = \epsilon_m^{\text{exp}}(\omega) + (\omega_p^{\text{exp}})^2 / (\omega^2 + i\omega\gamma^{\text{exp}})$ , where  $\omega_p^{\text{exp}}$  and  $\gamma^{\text{exp}}$  are the experimentally determined plasma frequency and phenomenological free-electron inelastic scattering rate, respectively. The parameters used to characterize silver, gold, and copper are specified in Table 1, while the isolated  $\epsilon_b$  are presented in Fig. 7.

Using the ALP-RPA model, we follow the prescription outlined in Appendix A.3 to extract the Feibelman  $d$ -parameters associated with noble metal surfaces having specific crystallographic orientations (Fig. 1). More specifically, after computing the reflection coefficient in the ALP-RPA formalism, the  $d$ -parameters are extracted by fitting Eq. (1) while employing a Drude-like dielectric function of the form

$$\epsilon_m(\omega) = \epsilon_b(\omega) - \frac{(\omega_p^{\text{ALP}})^2}{\omega(\omega + i\gamma^{\text{exp}})}, \quad (4)$$

where  $\omega_p^{\text{ALP}}$  is the plasma frequency obtained by fitting Eq. (1) in the  $Q \rightarrow 0$  limit to the ALP-RPA model. The employed values of

$\omega_p^{\text{ALP}}$ , which are related to the electron density computed from the ALP by populating electronic states of a semi-infinite metal film until the Fermi energy converges to its experimentally determined value, are listed in Table 3.

To better distinguish the quantum effects directly related with crystallographic facets, the  $d_{\perp}$ -parameters extracted from the ALP-RPA in Fig. 1 are contrasted with those obtained within the specular reflection model (SRM), first proposed by Ritchie and Marusak to study nonlocal effects impacting the dispersion of surface plasmons [49], and later generalized by others to deal with more complex structures [21,29,49–51]. The SRM—also known as the semiclassical infinite barrier model (SCIB)—incorporates *bulk* spatial dispersion (i.e., nonlocality or  $Q$ -dependent response) but assumes a bulk, homogeneous electron gas, and thus neglects both *surface* response and atomic corrugations captured in the ALP-RPA model. In the case of the (100) orientation and the SRM, the absence of surface currents for charge-neutral materials yields  $d_{\parallel} = 0$  [36,39]. Here, and for (111) surfaces alone, we introduce  $d_{\parallel}$  heuristically to incorporate the response due to the presence of Shockley SSs in (111) facets—as explained in Appendix A.2; when extracting  $d_{\perp}$  for the (111) facets, we explicitly omit intraband transitions involving SSs to avoid double-counting the effect of the 2DEG. The Feibelman  $d_{\perp}$ -parameters presented in Fig. 1 clearly distinguish the surface response akin to distinct metal crystallographic facets, i.e., different facets yield different  $d$ -parameters. In particular, these differences are more discernable at low energies ( $\hbar\omega < 1$  eV) and at energies around  $\hbar\omega_{\text{sp}}^{\text{cl}} = \hbar\omega_p / \sqrt{\epsilon_b(\omega_{\text{sp}}^{\text{cl}}) + \epsilon_d}$  where the classical nonretarded surface plasmon is spectrally centered.

The  $d$ -parameter data presented in Fig. 1 show that  $\text{Re}\{d_{\perp}\} < 0$  for  $\omega \lesssim \omega_{\text{sp}}^{\text{cl}}$ , thus indicating an inward spill of the induced electron density in noble metals, as opposed to the spill-out exhibited by simple (i.e., jellium) metals [39,54]. Such spill-in behavior in noble metals has been reported in numerous experimental studies, and has been attributed to the dielectric screening from core electrons [39]. Importantly, the approach we introduce here to extract  $d$ -parameters from optical response calculations (namely, through fits to the ALP-RPA-obtained reflection coefficient; see Appendix A) reproduces the correct spill-in behavior ( $\text{Re}\{d_{\perp}\} < 0$ ), in agreement with direct ALP-RPA computations of the induced charge density, where the centroid of the induced charge density (corresponding to  $\text{Re}\{d_{\perp}\}$ ) is indeed found to be located *inside* the metal (Fig. S1). As we show in the following, the advantage of the  $d$ -parameter formalism lies in its applicability to describe the optical response of not only semi-infinite metallic films, but also of more intricate noble metal morphologies.

### A. Nonretarded Surface Plasmon Dispersion

In possession of the  $d$ -parameters associated with various noble metal surfaces and their crystal facets, along with the analytical expression of Eq. (1), we reproduce the nonretarded surface plasmon dispersion (given by the poles of  $r_{\text{dm}}$ ) obtained directly from the ALP-RPA model. While the ALP method actually describes a crystalline metal film of finite thickness, we obtain well-converged results for  $N \gtrsim 50$  monolayers. Figure 2(a) shows the loss function (via  $\text{Im}\{r\}$ ) for silver with a (111) crystallographic orientation in the ALP-RPA model as a function of in-plane wave vector ( $Q$ ) and energy; peaks in  $\text{Im}\{r\}$  indicate the surface plasmon dispersion, which tends toward zero frequency for small  $Q$ , in accordance with Eq. (3) for a film of finite thickness. Figures 2(b) and 2(c) display the nonretarded surface plasmon dispersion for Ag and Au, obtained from the ALP-RPA approach (colored dots) along with the  $d_{\perp}$ -parameter formalism (solid curves), together with available experimental data [52,53]. Here, the  $d_{\perp}$ -parameter results have been extracted by comparing Eq. (1) with the ALP-RPA-computed reflection coefficient in the thick-film limit; this procedure, however, needs to be carried out judiciously, as the conditions  $QL \gg 1$  and  $Q|d_{\alpha}| \ll 1$  (and provided that  $L \gg |d_{\alpha}|$ ) must be simultaneously fulfilled. More specifically, the extracted

$d$ -parameter-corrected reflection coefficient reproduces the plasmon dispersion (to leading order in  $Qd_{\alpha}$ ) directly computed from the ALP-RPA, provided that the aforementioned conditions are satisfied.

Chiefly, our results show that the optical response of a metal surface is determined by the surface's specific crystallographic orientation and can be well described in terms of the Feibelman  $d_{\perp}$ -parameter for silver surfaces, as evidenced by the nearly overlapping dispersion relations obtained via the ALP-RPA model and through the corresponding  $d$ -parameters. We can further distinguish the surface plasmon dispersion for different crystallographic facets of the same metal, even in the  $Q \rightarrow 0$  limit [as a consequence of Eq. (4)], which can be attributed to differences in their electronic band structure. Notably, the  $d$ -parameter-corrected response of the Ag(111) surface—obtained from both the ALP-RPA and the SRM—is in good agreement with experiment. However, for the Au(111) surface, this is not the case, because the determination of the gold surface plasmon dispersion is complicated by the onset of broadening in the loss function at low  $Q$ , as we show in Fig. S2; the situation is further compounded for copper, where no clear maximum emerges in either the response described by Eq. (1) with  $d$ -parameters or the direct ALP-RPA calculation, with only the simpler SRM exhibiting well-defined maxima (see Fig. S3 for a comparison of the quantum-corrected surface plasmon dispersion relation, using the  $d$ -parameters obtained in SRM formalism, with experimental measurements based on attenuated total reflection of polycrystalline copper).

It is instructive to note at this point that, from Eq. (1), the nonclassical spectral correction to the nonretarded surface plasmon frequency—keeping only terms up to first order in  $Qd_{\alpha}$ —is given by [21,38,39]

$$\text{Re}\{\omega_{\text{sp}}\} \approx \omega_{\text{sp}}^{\text{cl}} \left[ 1 - \frac{\epsilon_{\text{d}}}{\epsilon_{\text{b}}(\omega_{\text{sp}}^{\text{cl}}) + \epsilon_{\text{d}}} Q \text{Re}\{d_{\perp} - d_{\parallel}\} \right], \quad (5)$$

where, as mentioned earlier,  $\omega_{\text{sp}}^{\text{cl}} \equiv \text{Re}\left\{\omega_{\text{p}}/\sqrt{\epsilon_{\text{b}}(\omega_{\text{sp}}^{\text{cl}}) + \epsilon_{\text{d}}}\right\}$  is the classical nonretarded surface plasmon frequency [21,29].

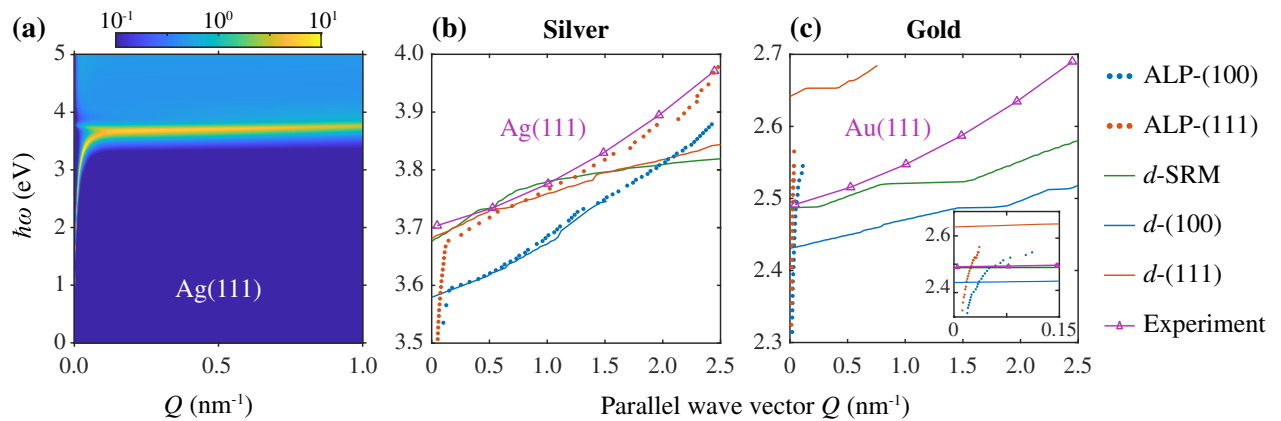


**Fig. 2.** Nonclassical surface plasmon dispersion. (a) Loss function, via  $\text{Im}\{r\}$ , of a thick film consisting of  $N = 100$  Ag(111) layers (i.e., effectively in the semi-infinite limit) obtained within the ALP-RPA model. (b), (c) Dispersion relations of the indicated metals and facets as determined from maxima in their computed loss functions; we extract the maxima of  $\text{Im}\{r\}$  directly from ALP-RPA calculations (color-coded points), while the dispersion of the  $d$ -parameter-corrected model (solid curves) is given by the poles of the denominator of  $r_{\text{dm}}$  obtained by fitting Eq. (1) to the ALP-RPA-computed reflection coefficient. The triangular symbols represent experimental data for Ag(111) [52] and Au(111) [53].

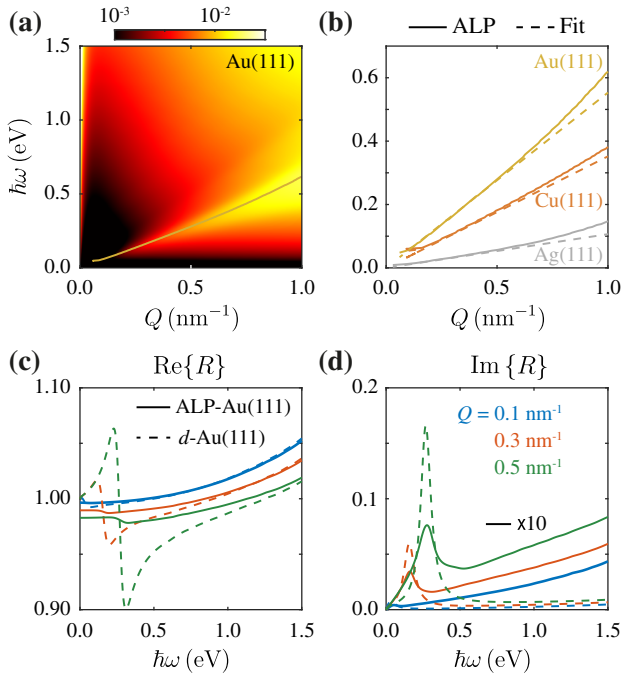


**Fig. 3.** Acoustic surface plasmons in (111) noble metal surfaces. (a) Loss function,  $\text{Im}\{r\}$ , associated with a Au(111) surface computed within the ALP-RPA model for a thick film in the semi-infinite limit (specifically, for  $N = 100$ ). (b) Acoustic surface plasmon dispersion obtained via the ALP-RPA model (solid line) and fitting (dashed line) to the linear dispersion  $\omega = v_\phi Q$ , with phase velocities  $v_\phi$  detailed in Table 3. (c) Real and (d) imaginary parts of the reflection coefficient of a Au(111) thick film ( $N = 100$  layers; indistinguishable from a semi-infinite metal) determined using both the ALP-RPA model (solid curves) and by employing the corresponding  $d$ -parameters (dashed curves) for selected parallel wave vectors  $Q$  [indicated by the color-matched legend in (d)].

## B. Acoustic Surface Plasmons Due to Shockley Surface States

At low frequencies, a feature exhibiting a nearly linear dispersion emerges in the loss function associated with (111)-faceted metal surfaces, indicating the existence of acoustic surface plasmons arising from the presence of Shockley SSs [29,32,55–58]. Figure 3 shows the loss function of a Au(111) surface, which in the low-frequency regime is marked by the presence of a well-defined—but relatively broad—feature associated with its acoustic surface plasmon [c.f. scales of Figs. 3(a) and 2(a)]. Next, we present the dispersion relation of acoustic surface plasmons akin to the Au(111), Ag(111), and Cu(111) surfaces obtained within the ALP-RPA framework (solid curves), and whose slope—corresponding to the acoustic surface plasmon velocity—is then determined through a linear fit (dashed curves); see Table 2. Note that the intrinsic acoustic surface plasmons supported by noble metal surfaces of well-defined crystallographic orientation have been characterized experimentally under different conditions: for Au(111), a phase velocity  $v_\phi/v_{2D} = 1.7$  was observed in Ref. [59], while a value  $v_\phi/v_{2D} \approx 0.8$  was reported at 78 K in Ref. [60]. The extracted value in the present work is close to unity (see Table 2).

In principle, the Shockley 2DEG supported by the (111)-facets can be accounted for through the Feibelman  $d_\parallel$ -parameter (since it is formally tantamount to a surface conductivity). Here, we exploit this and introduce, in an *ad hoc* fashion, a heuristic expression for  $d_\parallel$  (see Appendix A.2 for details). We emphasize here that, because

**Table 2.** Characterization of Acoustic Plasmons Originating from Shockley Surface States<sup>a</sup>

Material	$E_F - \epsilon_{SS}^\perp$ (eV)	$m^*(SS)/m_e$	$v_{2D}/c$	$v_\phi/v_{2D}$	$\hbar\gamma_{2D}$ (meV)
Ag(111)	0.026	0.40 [61]	$5.04 \times 10^{-4}$	1.0690	27.5
Au(111)	0.525	0.26 [61]	$2.81 \times 10^{-3}$	0.9971	83.7
Cu(111)	0.356	0.41 [61]	$1.84 \times 10^{-3}$	0.9676	118.1

<sup>a</sup>We parametrize the (111) surface state (SS) of a specified noble metal by its energy  $\epsilon_{SS}^\perp$  below the Fermi energy  $E_F$ , effective mass  $m^*$ , and Fermi velocity  $v_{2D}$ . The resulting acoustic plasmons are characterized by their phase velocity  $v_\phi$  and phenomenological damping  $\hbar\gamma_{2D}$ .

we account for the 2DEG heuristically, intraband transitions involving SSs are omitted in the ALP-RPA-based  $d_\perp$  calculations (thereby avoiding double-counting that contribution). Then, in possession of both  $d_\perp$  and  $d_\parallel$ , we employ Eq. (1) to reproduce the optical response calculations obtained using the ALP-RPA model. As observed in Figs. 3(c) and 3(d), where the real and imaginary parts of the reflection coefficient for Au(111) are compared for different values of  $Q$ , the agreement of the spectral positions is satisfactory for small  $Q$  (where the  $d$ -parameter formalism is valid), although the amplitudes of these already weak features are not well reproduced.

## C. Nonclassical Optical Response of Ultrathin Metal Films

The practical utility of the  $d$ -parameter framework for mesoscale electromagnetism becomes apparent by recognizing that, once obtained for a specific dielectric–metal interface, they can be readily incorporated in a broad range of optical response calculations, either via  $d$ -parameter-corrected scattering coefficients [21,38] or through  $d$ -parameter-modified boundary conditions [21,41,42].

As a concrete example, we now investigate the nonclassical optical response of ultrathin silver films comprising  $N$  (111) atomic monolayers. Figures 4(b) and 4(c) show that the loss function calculated within the ALP-RPA model for ultrathin silver films (with thicknesses  $N = 20$  and  $N = 5$ ) is dominated by the surface plasmons supported by the films. Incidentally, the plasmon dispersion relation obtained from the ALP-RPA model resembles that obtained in a classical FP description. Figures 4(d)–4(g) compare the spectral dependence of the reflection coefficient around the surface plasmon resonance for selected in-plane wave vectors, contrasting results from the ALP-RPA model with those from FP models that include or neglect the  $d_\perp$ -parameter correction. For small values of a parallel wave vector ( $Q = 0.1 \text{ nm}^{-1}$ ), quantum corrections do not strongly impact the position and width of the plasmon resonance; at larger in-plane momenta ( $Q = 0.8 \text{ nm}^{-1}$ ), where the plasmon resonance approaches that of a semi-infinite film, the resonance features in the classical FP model exhibit differences from those in the ALP-RPA calculation, which are captured by the  $d$ -parameters. The excellent agreement between the calculated curves based on the  $d$ -parameter and ALP-RPA frameworks underscores how the optical response obtained analytically using Eq. (3) together with the Feibelman  $d$ -parameters [see Eqs. (1) and (2)] accurately accounts for quantum effects impacting the film’s electromagnetic response. Curiously, the optical response for extremely thin Ag films, even down to  $N = 5$  atomic planes (except for low wave vectors, such as  $Q = 0.1 \text{ nm}^{-1}$  in the  $N = 5$  case, presumably because the condition  $QL \gtrsim 1$  is not fulfilled), appears to be well reproduced by the  $d$ -parameter-corrected

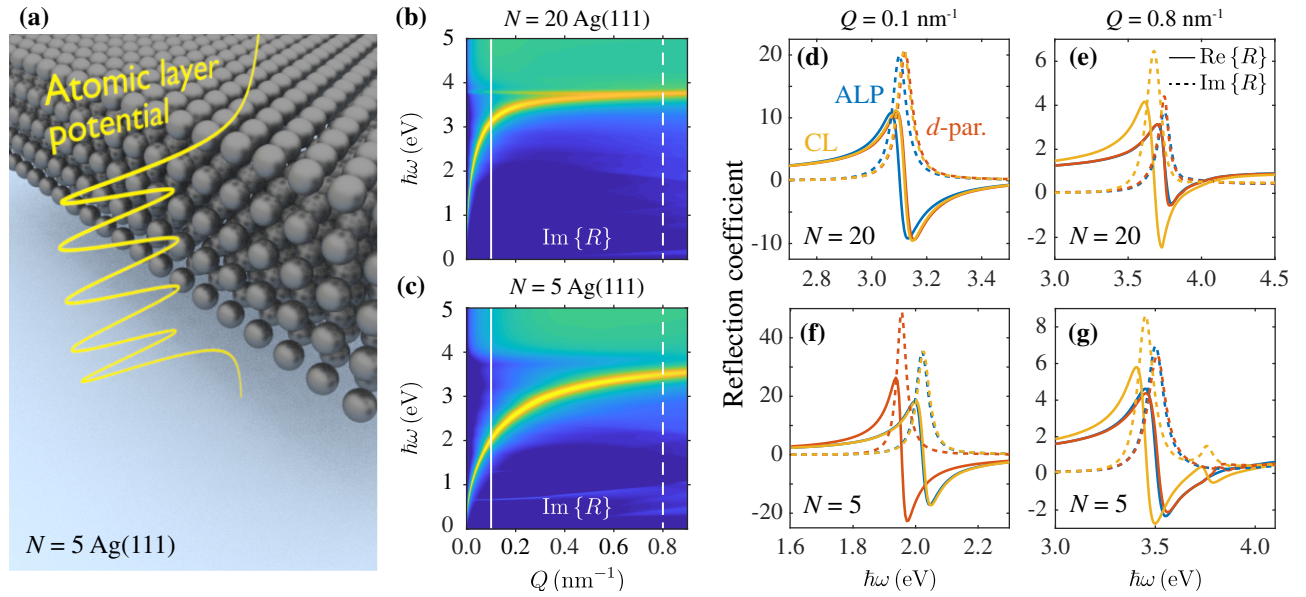


**Fig. 4.** Nonclassical optical response of ultrathin metal films. (a) Schematics of Ag(111) film corresponding to  $N = 5$  monolayers. (b), (c) Plasmon dispersion relation, shown as a feature in the loss function  $\text{Im}\{R\}$ , for Ag(111) films corresponding to (b)  $N = 20$  and (c)  $N = 5$  Ag monolayers using the ALP-RPA model. The white vertical lines in each figure select the loss function at  $Q = 0.1 \text{ nm}^{-1}$  (solid line) and  $Q = 0.8 \text{ nm}^{-1}$  (dashed line), for which the corresponding reflection coefficient  $R$  near the plasmon resonance is shown in panels (d) and (e), respectively, for  $N = 20$  monolayers, and similarly in panels (f) and (g) for  $N = 5$ . (d)–(g) Real (solid curves) and imaginary (dashed curves) parts of the reflection coefficient  $R$  computed in the ALP-RPA (ALP, blue curves) and compared to the Fabry–Perot model of Eqs. (1)–(3) for calculations including the extracted  $d_{\perp}$  ( $d$ -par., red curves) and the purely classical (CL, yellow curves) result obtained by setting  $d_{\perp} = d_{\parallel} = 0$ .

thin film reflection coefficient, although the application of the  $d$ -parameters to describe such extremely thin films ( $N \lesssim 10$ ) lies in the borders of the regime of validity (i.e., subjected to  $L \gg |d_{\alpha}|$ ) of the  $d$ -parameter formalism for few-atom-thick films.

#### D. Graphene Next to Crystallographically Faceted Metal Films: Acoustic Graphene Plasmons

We consider the “extrinsic” acoustic plasmons produced by the hybridization of a closely spaced graphene layer with a crystalline metal film. Unlike the “intrinsic” acoustic plasmons supported by the (111)-facets, graphene’s optoelectronic tunability [62] provides an additional knob to actively modulate the optical response of the emerging low-energy acoustic plasmon modes with linear dispersion [63]. The experimental capability to position graphene within  $\sim 1 \text{ nm}$  of a noble metal layer has been spurring enticing explorations of extreme light concentration within the gap region [21,40,64–66], which could be further improved by employing crystalline noble metals [44]. In what follows, we summarize the semi-analytical FP description of the optical response based on the extracted  $d$ -parameters.

For a zero-thickness 2D graphene monolayer, the reflection and transmission coefficients in the nonretarded limit [21,62,67] read

$$r_{\text{gr}}^{2\text{D}} = \frac{1}{1 - i\omega/(2\pi Q\sigma)}, \quad t_{\text{gr}}^{2\text{D}} = 1 - r_{\text{gr}}^{2\text{D}},$$

where  $\sigma(Q, \omega)$  is the nonlocal conductivity of graphene, which we treat here at the level of the nonlocal RPA [21,62,68,69] (using Mermin’s prescription for the relaxation-time approximation, which conserves a local particle number [70]; we take  $\tau = 500 \text{ fs}$ ).

Similar to Eq. (3), we compute the reflection coefficient of an extended graphene sheet on top of a semi-infinite metal via the FP model as

$$R = r_{\text{dm}} + \frac{t_{\text{gr}}^2 r_{\text{dm}} e^{-2Qs}}{1 - r_{\text{gr}} r_{\text{dm}} e^{-2Qs}}, \quad (6)$$

where  $s$  stands for the graphene–metal separation, and  $r_{\text{gr}}$  and  $t_{\text{gr}}$  are the (nonretarded) reflection and transmission coefficients of graphene, respectively. In our calculations, we follow the prescription of Ref. [55] to account for the spatial dependence of the carbon 2p orbitals  $\varphi_{2p}(\mathbf{r})$  extending outwards from the graphene monolayer plane, leading to the corrected graphene reflection and transmission coefficients  $r_{\text{gr}} = r_{\text{gr}}^{2\text{D}} C_{\text{gr}}^2 e^{-Qd_{\text{gr}}}$  and  $t_{\text{gr}} = t_{\text{gr}}^{2\text{D}} C_{\text{gr}}^2 e^{-Qd_{\text{gr}}}$ , where  $d_{\text{gr}} = 0.33 \text{ nm}$  is the interlayer spacing of graphite and  $C_{\text{gr}}$  is a coupling factor defined in Ref. [55]. Taking into account the aforementioned *effective* graphene thickness, the separation distance  $s$  actually corresponds to the distance between the edge of the graphene and the metal surface, i.e.,  $s = 0$  corresponds to a *finite* distance  $d_{\text{gr}}/2$  between the graphene center and the metal surface.

Acoustic graphene plasmons emerge when a graphene sheet is placed near a metal [21,64–66], and whose signature is a prominent low-energy linear dispersion feature in the reflection coefficient [Fig. 5(a)]. For the considered graphene–Au(111) surface, the extrinsic acoustic plasmons are characterized as before by  $\omega = v_{\text{gr}} Q$ , with  $v_{\text{gr}}$  denoting the associated group velocity; in such a heterostructure,  $v_{\text{gr}}$  is determined by graphene’s Fermi energy  $E_{\text{F}}$  and the graphene–metal spacing  $s$ , as illustrated in Fig. 5(b). Figure 5(c) reveals that neither the choice of model nor the considered crystalline facet strongly influences the acoustic plasmon dispersion characteristics. At low energies, the noble metals are all good conductors that effectively screen the graphene plasmon and render its dispersion acoustic. We remark, however, that, for the same heterostructure, the dispersion relation of the higher energy hybrid plasmon mode is indeed dominated by the

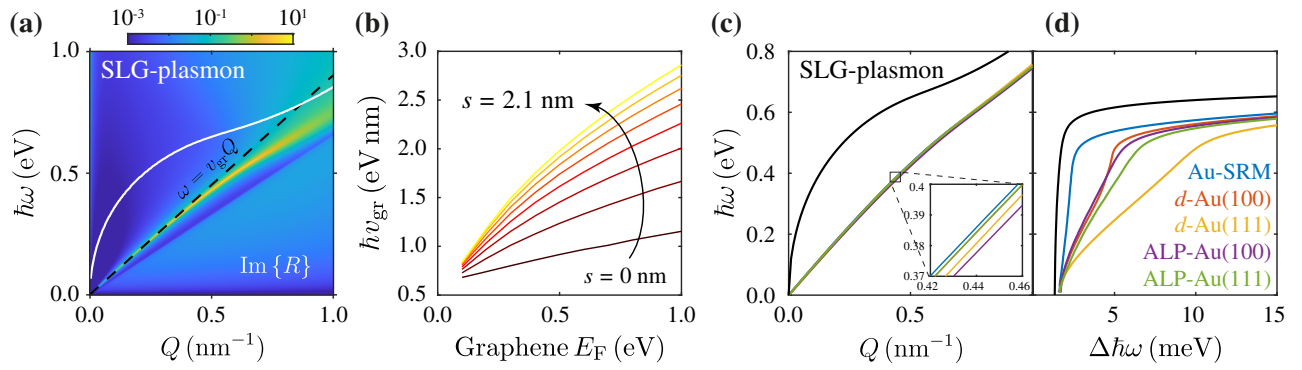


**Fig. 5.** Acoustic graphene plasmons on a Au(111) surface. (a) Loss function,  $\text{Im}\{R\}$ , for single-layer graphene (SLG) doped to a Fermi energy  $E_F = 0.5$  eV and deposited directly on top of a semi-infinite metal Au(111) surface (the latter described within the ALP-RPA model). The white curve corresponds to plasmons in free-standing SLG, and the black dashed curve is a linear fit to the resulting acoustic plasmon characterized by an acoustic velocity  $v_{\text{gr}}$ . (b)  $v_{\text{gr}}$  computed as a function of doping while varying the separation distance from  $s = 0$  nm to  $s = 2.1$  nm in steps of 0.3 nm. (c) Acoustic plasmon dispersion for a graphene-gold heterostructure computed using the various gold film models, as indicated in the legend in (d), which depicts the associated linewidths. In (c) and (d), the black solid line is a reference for isolated SLG with  $E_F = 0.5$  eV.

metal's properties [44]. However, inspection of the linewidths of the acoustic plasmon in Fig. 5(d) reveals a substantial dependence on the quantum-mechanical effects arising from the various crystalline facets, which is underlined by the underestimation of spectral widths in the SRM [44]. In particular, the obtained results suggest that crystalline Au(111) gives rise to additional surface-enhanced damping when compared to Au(100), presumably due to the presence of an SS, and warranting further studies of the acoustic plasmons in such heterostructures.

### E. Crystallographically Faceted Nanoparticles

Going beyond planar, layered media, we explore the role of crystallographic orientation in faceted noble metal nanoparticles (NPs). The optical response of metallic NPs is dominated by the localized surface plasmon (LSP) resonances supported by it, the most prominent of which are typically those of dipolar character, as they can couple to far-field radiation. As the NP size is reduced towards nanometric dimensions, the ensuing NP's surface-to-volume ratio grows and thus leads to successively more pronounced non-classical corrections associated with the NP's quantum surface response. To illustrate the importance of using the appropriate Feibelman  $d$ -parameters for determining the quantum surface-response associated with specific facets, we consider in Fig. 6(a) a realistically faceted silver NP. Any natural NP—especially those with characteristic dimensions  $\lesssim 10$ – $20$  nm—no matter how carefully synthesized, will always deviate from a perfect sphere as a consequence of its growth in a sequence of specific crystallographic planes [71]. The shape closest to a sphere is that of a truncated octahedron, characterized by large hexagonal (111) surfaces and smaller (100) facets, as depicted schematically in Fig. 6.

To compute the NP's nonclassical extinction cross-section  $\sigma_{\text{ext}}$ , we have implemented in a finite-element method (FEM) solver the mesoscopic  $d$ -parameter-corrected boundary conditions [21,38,41,42]. In practice, this is tantamount to the introduction of *surface* electric and magnetic currents (see Appendix A.3) characterized by the  $d$ -parameters presented in Fig. 1. Comparing with the classical spectra (red curves), it is clear that the effect of the  $d$ -parameters is to capture the nonlocal optical response of such a NP. As expected for silver, the spectra are shifted toward higher energies as a result of an inward shift ( $\text{Re}\{d_{\perp}\} < 0$ ) of the

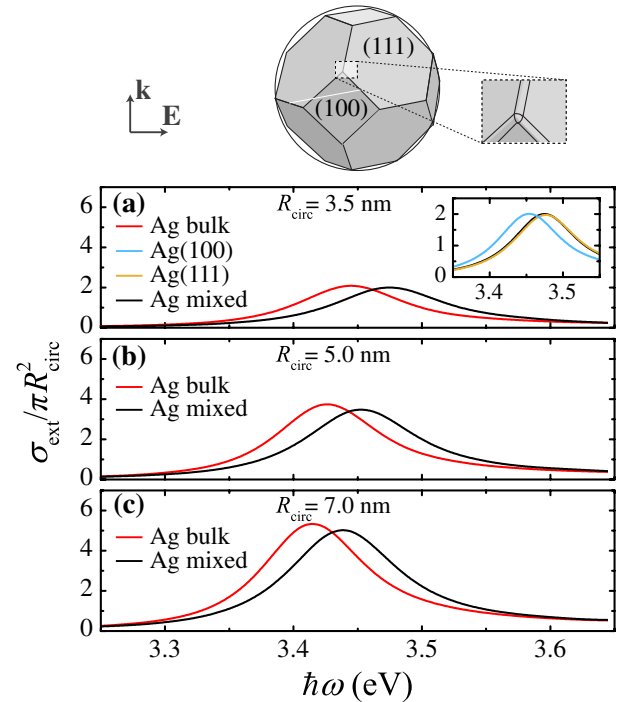


**Fig. 6.** Extinction spectra for a Ag truncated octahedra including quantum surface corrections. Optical extinction cross-section (normalized to the geometric cross-section area) of the circumscribed sphere  $R_{\text{circ}}$  for Ag truncated octahedra with  $R_{\text{circ}} = 3, 5,$  and  $7$  nm (a, b, and c respectively), as shown in the schematics at top. Red curves correspond to the response of bulk Ag (classical with no  $d$ -parameters), and black curves to facets (100) and (111) described by their corresponding  $d$ -parameters shown in Figs. 1(a) and 1(b). The blue and yellow curves in the inset of (a) show the corresponding spectra if the entire particle is described entirely by the Feibelman parameters of (100) and (111) facets, respectively.

screening charges. Studying different NP sizes, from 3 to 7 nm in radius (meaning here the circumscribed radius  $R_{\text{circ}}$ ; see Fig. 6), a consistent trend is observed, with the resonance broadening (as a result of increased surface-assisted Landau damping) and undergoing stronger blueshifts as the size decreases, which is compatible with the predictions of nonlocal hydrodynamics [50,72,73], and

also in accordance with electron energy-loss spectroscopy (EELS) experiments [74–77]. The observed behavior is attributed mainly to the (111) facets—as shown in the inset of Fig. 6(a)—where blue and yellow curves show the corresponding spectra assuming that the entire NP is described solely by the  $d$ -parameters akin to the (100) or (111) surface, respectively (see Dataset 1, Ref. [78]). Naturally, since the associated surface area of the (100) facets is smaller, and their corresponding Feibelman parameters are significantly lower in magnitude than those of the (111) surface, the former induce only a small frequency shift in the spectra. Then, since the main effect is due to the (111) facets, the corresponding spectrum almost coincides with the “mixed” one, where each facet is described by its own parameters. It is also worth noting that, because the truncated octahedron constitutes a highly symmetric shape, the optical response of such NPs resembles that of spheres, and thus changing the angle of incidence is not expected to lead to significant differences.

### 3. CONCLUSION

The inherently large losses exhibited by noble metals are often regarded as the “Achilles heel” of nano-optical functionalities based on plasmonics, motivating intensive efforts to identify new material platforms that can support long-lived polaritons. Crystalline noble metal films constitute one appealing possibility that is now becoming increasingly available. Here, we have introduced quantum surface-response corrections encoded in the Feibelman  $d$ -parameters obtained from quantum-mechanical optical response calculations (namely, using the ALP-RPA model) of crystalline noble metals. We have shown that the  $d$ -parameters for gold, silver, and copper surfaces tabulated here with specific crystallographic orientations can be straightforwardly incorporated in analytical models as well as in computational electromagnetic solvers for computing the nonclassical optical response of various nanoplasmonic systems of interest that contain these facets. In particular, the  $d$ -parameters associated with silver, for which screening by core electrons and interband transitions emerge at higher energies, are found to faithfully reproduce atomistic quantum-mechanical calculations, while further explorations (both theoretical and experimental) of plasmon dispersion relations in crystalline Au and Cu are needed to consolidate their surface-response functions. Nevertheless, we envision that the  $d$ -parameters reported here can be widely deployed to describe quantum surface effects in crystalline noble metal surfaces that are actively explored for novel nanophotonic functionalities and applications. Our prescription for extracting the Feibelman  $d$ -parameters directly from optical response calculations of metal surfaces is versatile and can be applied to various plasmonic nanostructures with different geometries and architectures, and could fuel further explorations of quantum nonlocal phenomena at dielectric–metal interfaces in both theory and experiment.

### APPENDIX A: MICROSCOPIC SURFACE-RESPONSE FUNCTIONS: FEIBELMAN $d$ -PARAMETERS

The surface-response functions introduced by Feibelman [21,36,39],  $d_{\perp}$  and  $d_{\parallel}$ , are formally given, respectively, by the first moment of the quantum mechanical induced charge density ( $\rho_{\text{ind}}$ ) and of the normal derivative of the parallel component of the corresponding current density ( $J_x^{\text{ind}}$ ) [21,36–38],

$$d_{\perp}(\omega) = \frac{\int_{-\infty}^{\infty} dz z \rho^{\text{ind}}(z, \omega)}{\int_{-\infty}^{\infty} dz \rho^{\text{ind}}(z, \omega)}, \quad (\text{A1a})$$

$$d_{\parallel}(\omega) = \frac{\int_{-\infty}^{\infty} dz z \frac{\partial}{\partial z} J_x^{\text{ind}}(z, \omega)}{\int_{-\infty}^{\infty} dz \frac{\partial}{\partial z} J_x^{\text{ind}}(z, \omega)}, \quad (\text{A1b})$$

in the long-wavelength limit. The Feibelman  $d$ -parameters can be rigorously incorporated in electrodynamic problems by appropriately modifying the boundary conditions at a given dielectric–metal surface [21,38,42], in both analytical treatments [21,37,38,41] and numerical implementations [41,42].

In the following, we abstract the contributions from *bulk* spatial dispersion (relevant for any metal surface with a compressible electron gas) and *surface* contributions associated with the presence of Shockley SSs [relevant to the (111) noble metal surfaces].

### 1. CONTRIBUTIONS FROM BULK SPATIAL DISPERSION

The surface-response functions associated with the spatial dispersion (nonlocal response) of the bulk response functions of the metal [i.e., the wave vector dependence of the *bulk* dielectric function,  $\epsilon_{\perp}(k, \omega)$ ], can be incorporated in the  $d$ -parameters, for example, via the SRM using [21,29,51]

$$d_{\perp}^{\text{SRM}} = -\frac{2}{\pi} \frac{\epsilon_m \epsilon_d}{\epsilon_m - \epsilon_d} \int_0^{\infty} \frac{dk}{k^2} \left[ \frac{1}{\epsilon_{\perp}(k, \omega)} - \frac{1}{\epsilon_m} \right], \quad (\text{A2a})$$

$$d_{\parallel}^{\text{SRM}} = 0. \quad (\text{A2b})$$

We note that the vanishing of  $d_{\parallel}$  is a consequence of the charge-neutral interface [39]. Below, we discuss how this is changed (heuristically) in the presence of a Shockley SS.

### 2. CONTRIBUTIONS FROM SHOCKLEY SURFACE STATES

We now consider the effect of a Shockley SS, while for simplicity leaving out the response associated with the spatial dispersion of the bulk states. We note that, with our sign convention of the surface-normal, the surface conductivity  $\sigma_{2D}$  is related to the Feibelman  $d_{\parallel}$  parameter as  $\sigma_{2D}(\omega) = -i\omega\epsilon_0(\epsilon_m - \epsilon_d)d_{\parallel}(\omega)$  [21]. Furthermore, in the nonretarded limit, the 2D plasmon dispersion relation associated with  $\sigma_{2D}$  is generally given by  $Q(\omega) = i\omega\epsilon_0(\epsilon_m + \epsilon_d)/\sigma_{2D}(\omega)$  [21]. Anticipating that we have a Shockley SS that supports an acoustic plasmon [30], corresponding to a dispersion relation  $\sqrt{\omega(\omega + i\gamma_{2D})} = v_{\phi} Q$ , we thus find the connection between this phase velocity  $v_{\phi}$  and the “effective” Feibelman parameters to be of the form

$$d_{\perp}^{\text{SS}} = 0, \quad (\text{A3a})$$

$$d_{\parallel}^{\text{SS}} = -\frac{\epsilon_m + \epsilon_d}{\epsilon_m - \epsilon_d} \frac{v_{\phi}}{\sqrt{\omega(\omega + i\gamma_{2D})}}. \quad (\text{A3b})$$

For low frequencies ( $\omega \ll \omega_p$ ), this simplifies to  $d_{\parallel}(\omega) \simeq v_{\phi}/\sqrt{\omega(\omega + i\gamma_{2D})}$ , and asymptotically vanishes at high frequencies. When implemented in the mesoscopic boundary conditions for the electrostatics, these Feibelman parameters—by construction—support an acoustic plasmon with the desired phase velocity. Considering the poles of the scattering coefficients [see Eqs. (1) and (2)] together with Eq. (A3), we obtain

$$0 = \epsilon_m + \epsilon_d - (\epsilon_m - \epsilon_d) Q(d_{\perp} - d_{\parallel})$$

$$= (\epsilon_m + \epsilon_d) \left( 1 - \frac{v_{\phi} Q}{\sqrt{\omega(\omega + i\gamma_{2D})}} \right), \quad (\text{A4})$$

and we indeed find two decoupled solutions: the “classical” surface plasmon resonance (defined by  $\epsilon_m + \epsilon_d = 0$ ) and the (added *ad hoc*) acoustic one with  $\sqrt{\omega(\omega + i\gamma_{2D})} = v_{\phi} Q$ . Table 2 gathers the obtained phase velocities by fitting the acoustic surface plasmon featured in the optical response [Fig. 3(a)], and the damping  $\gamma_{2D}$  by associating the resonance to the width of a Lorentzian; specifically, the widths have been computed numerically from the second derivative of the imaginary part of the reflection coefficient to remove the background contribution.

### 3. EXTRACTION OF THE $d$ -PARAMETERS FOR CRYSTALLINE METAL SURFACES

We describe crystalline metal films quantum mechanically, computing their optical response at the level of the RPA following the procedure detailed in Ref. [44]. As explained therein, metal films are considered to have translational symmetry in the  $\mathbf{R} = (x, y)$  plane, so that their electronic wave functions are amenable to expansion in a plane wave basis according to  $\Psi_{j, \mathbf{k}_{\parallel}}(\mathbf{r}) = A^{-1/2} e^{i\mathbf{k}_{\parallel} \cdot \mathbf{R}} \varphi_j(z)$ , with  $A$  denoting the normalization area,  $\mathbf{k}_{\parallel}$  the 2D electron momentum, and  $\varphi_j(z)$  the spatial dependence of state  $j$  in the quantization direction  $z$ . The latter quantity is obtained by solving the eigenvalue problem  $\mathcal{H}\varphi_j(z) = \hbar\epsilon_j^{\perp} \varphi_j(z)$  to obtain the associated energy eigenvalues  $\hbar\epsilon_j^{\perp}$  of the 1D Hamiltonian  $\mathcal{H} = -\hbar^2 \partial_z^2 / 2m_e + V(z)$  determining the band dispersion  $\hbar\epsilon_{j, \mathbf{k}_{\parallel}} = \hbar^2 \mathbf{k}_{\parallel}^2 / 2m_e + \hbar\epsilon_j^{\perp}$ . The 1D potential  $V(z)$ , herein referred to as the ALP, is selected from those reported in Ref. [43] that characterize faceted metals of thickness  $L$  composed of  $N$  atomic planes stacked along the  $z$  direction with interlayer spacing  $a_s$  (naturally,  $L$  is an integer multiple of  $a_s$ ).

Electronic bands are populated by successively filling the lowest bands until the effective bulk electronic density  $n_{\text{eff}}$  is reached, thereby determining the Fermi energy  $E_F$  as

$$E_F = \left( \sum_{j=1}^M m_j^* \right)^{-1} \left( n_{\text{eff}} \hbar^2 \pi + \sum_{j=1}^M m_j^* \epsilon_j^{\perp} \right), \quad (\text{A5})$$

where the sums over  $j$  terminate when  $\epsilon_M^{\perp} < E_F / \hbar < \epsilon_{M+1}^{\perp}$  (i.e.,  $j = M$  is the highest partially occupied band). The electronic densities  $n_{\text{eff}}$  are determined by imposing the experimentally established value of  $E_F$  for a given noble metal in the bulk limit (i.e., for

a sufficiently thick film). For consistency with experimental observations [82–84], we impose a linear variation in the effective mass of the parabolic bands as a function of their quantized energies  $\hbar\epsilon_j^{\perp}$  according to  $m_j^*/m_e = a\hbar\epsilon_j^{\perp} + b$ , thereby avoiding artifacts due to an unrealistic number of excitation channels for vertical transitions introduced by perfectly aligned parabolic bands; specific parameters used in our calculations are reported in Table 3—note that the SSs for (111) noble metal facets are assigned specific experimentally determined effective masses.

We characterize the optical response of noble metal films by the reflection coefficient  $R(\mathbf{Q}, \omega)$ , expressed as a function of the optical in-plane wave vector  $\mathbf{Q}$  and frequency  $\omega$ . Considering that the relevant length scales are far smaller than the involved optical wavelengths, we invoke the quasistatic approximation to compute the reflection coefficient in terms of electrostatic potentials as  $R = 1 - \phi(z)/\phi^{\text{ext}}(z)$ , where  $\phi = \phi^{\text{ext}} + \phi^{\text{ind}}$  is the sum of external and induced potentials, the former exciting the system and the latter computed following the ALP-RPA prescription reported in Ref. [44]. In principle, the RPA response function is constructed by summing over all possible transitions between electronic states; however, because the Shockley SS of the (111) surface is incorporated in  $d_{\parallel}$  following the *ad hoc* prescription in the previous section, the reflection coefficient used to extract  $d_{\perp}$  is computed by excluding intraband transitions involving (only) SSs, thereby avoiding double-counting such transitions.

Following the RPA description outlined in Ref. [55], we correct the Coulomb interaction to incorporate screening from core electrons using the experimentally extracted polycrystalline dielectric functions  $\epsilon_b(\omega)$  plotted in Fig. 7. The  $d_{\perp}$  associated with a given noble metal facet is extracted from ALP-RPA calculations of a sufficiently thick film, so that the optical response is converged with the number of atomic planes. More specifically, we obtain  $d_{\perp}$  by fitting Eq. (1) to the ALP-RPA reflection coefficient of the thick film, employing the corresponding bulk dielectric function  $\epsilon_m$  of Eq. (4). It should be noted that the bulk plasma frequency  $\omega_p^{\text{ALP}}$  for each metal surface orientation that enters Eq. (4) in the fitting is obtained from the ALP-RPA response of a finite film for a sufficiently small in-plane wave vector, e.g.,  $Q \sim 0.005 \text{ nm}^{-1}$ , so that nonlocal effects are safely neglected and the surface plasmon resonance is captured in an uncorrected (i.e., classical) FP description. This procedure enables a stable parametrization of the crystallographic bulk properties for each surface orientation when the contribution from the  $d$ -parameters is negligible. In practice, the surface plasmon for a finite film with  $N = 10 - 40$  atomic planes appears at lower energies than the surface plasmon for the semi-infinite film, and the associated resonance is undamped by

**Table 3. Characterization of Quantum Well States in Noble Metals<sup>a</sup>**

Material	$a(\text{eV}^{-1})$	$b$	$m^*(\text{SS})/m_e$	$m_0/m_e$	$n_{\text{eff}}/n_0$	$E_F$ (eV)	$\hbar\omega_p^{\text{ALP}}$ (eV)	$\hbar\gamma^{\text{exp}}$ (eV)
Ag(100)	−0.0817	0.2116	—	0.40 [79]	0.8710	−4.43 [43]	8.80	0.021
Ag(111)	−0.1549	−0.5446	0.40 [61]	0.25 [55]	0.8381	−4.63 [80,81]	9.19	0.021
Au(100)	−0.1068	−0.1802	—	0.24	0.9199	−5.47 [47]	8.67	0.071
Au(111)	−0.1660	−0.8937	0.26 [61]	0.26 [55]	0.9443	−5.50 [80,81]	9.88	0.071
Cu(100)	−0.0751	0.1078	—	0.34	0.9634	−4.59 [47]	11.38	0.103
Cu(111)	−0.1084	−0.3303	0.41 [61]	0.31 [55]	0.9285	−4.98 [47]	11.50	0.103

<sup>a</sup>The parameters defining the electronic bands of noble metals entering our optical response calculations are presented. Quantities  $a$  and  $b$  define the linear variation in effective mass for band  $j$  as a function of its associated energy  $\hbar\epsilon_j^{\perp}$ ; values for the Fermi energy  $E_F$ , the effective mass associated with surface states  $m^*(\text{SS})$ , and the effective mass for the bottom of the conduction band  $m_0$  are extracted from experimental reports, while the effective electron density  $n_{\text{eff}}$  is fitted to match  $E_F$ , thus fixing the plasma frequency  $\omega_p^{\text{ALP}}$ .

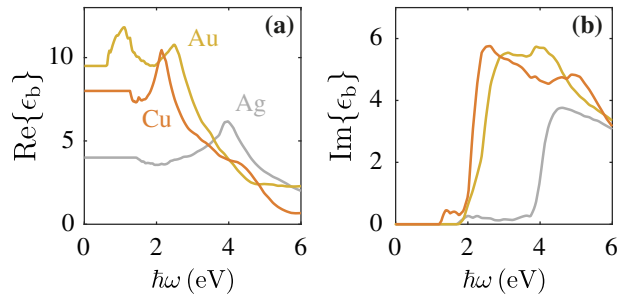


**Fig. 7.** Background dielectric function. (a) Real and (b) imaginary parts of  $\epsilon_b$  for the noble metals under consideration, obtained by subtracting  $-(\omega_p^{\text{exp}})^2/\omega(\omega + i\gamma^{\text{exp}})$  from the experimental tabulated data in Ref. [48]. See Table 3 for the characteristic parameters of each metal.

interband transitions, thereby giving rise to a well-defined peak (see, for instance, Fig. 4) from which  $\omega_p^{\text{ALP}}$  is obtained by fitting  $\epsilon_m = \epsilon_d(1 + r_{\text{dm}})/(1 - r_{\text{dm}})$  [c.f. (2) in the  $Q \rightarrow 0$  limit].

Once the bulk properties for each surface orientation are set, we construct  $d_{\perp}(\omega)$  at a given  $\omega$  by fitting Eqs. (1)–(3) for a given value of  $Q$  to the ALP-RPA-computed response. We maintain a large number of layers to avoid quantum finite-sized effects emerging in thin films ( $N \lesssim 10 - 20$  atomic layers). We then confirm that convergence is maintained with the calculated  $d_{\perp}(\omega)$  as the number of layers and/or parallel wave vectors is varied, where the latter condition is typically satisfied for  $0.3 \text{ nm}^{-1} < Q < 1.5 \text{ nm}^{-1}$ . After the parameters are obtained, they are applied to thick (Fig. 2) and thin films (Fig. 4). In (100)-facet metals, we have set  $d_{\parallel} = 0$ , whereas for the (111)-surface we employ the prescription of (4.1.2) (see Appendix A.2) to describe the intrinsic low-energy acoustic plasmon.

## APPENDIX B. FINITE-ELEMENT IMPLEMENTATION

To calculate the extinction spectra of the truncated octahedra, we used the commercial FEM solver COMSOL Multiphysics 5.4. As has been shown elsewhere [21,38,41,42], the Feibelman  $d$ -parameters can be incorporated in any computational method by adopting the so-called ( $d$ -parameter-corrected) mesoscopic boundary conditions. More specifically, the  $d$ -parameters introduce discontinuities in the parallel components of the electric and magnetic fields, which can be expressed through [21,38,42]

$$\hat{\mathbf{n}} \times (\mathbf{E}_2 - \mathbf{E}_1) = -d_{\perp} \hat{\mathbf{n}} \times [\nabla \hat{\mathbf{n}} \cdot (\mathbf{E}_2 - \mathbf{E}_1)], \quad (\text{B1a})$$

$$\hat{\mathbf{n}} \times (\mathbf{H}_2 - \mathbf{H}_1) = i\omega d_{\parallel} [\hat{\mathbf{n}} \times (\mathbf{D}_2 - \mathbf{D}_1) \times \hat{\mathbf{n}}], \quad (\text{B1b})$$

where  $\mathbf{E}_i$ ,  $\mathbf{H}_i$ , and  $\mathbf{D}_i$  are the electric, magnetic, and displacement fields, respectively, on side  $i$  of an interface between two media 1 and 2, and  $\hat{\mathbf{n}}$  is the unit vector normal to the interface. These conditions can be readily implemented in version 5.4 of COMSOL Multiphysics, through surface current and surface magnetic current densities, expressed through the down and up functions in COMSOL Multiphysics for the fields at sides 1 and 2. Since the expressions for these currents [right-hand sides of Eqs. (B1a) and (B1b)] contain the fields themselves, the problem needs to be solved iteratively, starting with the currents due to the incident plane wave. To calculate the scattering and absorption cross section, we need to integrate the Poynting flux of the scattered and

total field over a surface (a sphere) enclosing the NP, with a large enough radius ( $\sim 2 - 3$  nm more than  $R_{\text{circ}}$ ) to ensure that numerical noise due to the currents close to the surface will be minimum. For sharp-edged NPs—like the octahedra studied here—it is also necessary to introduce some rounding, to ensure that any spurious edge/corner modes will be absent. This is needed for the classical calculations (with  $d_{\perp} = d_{\parallel} = 0$ ) as well. For non-vanishing  $d$ -parameters, the additional damping they introduce smooths things nicely. However, for a direct comparison between the two cases, it is necessary to include the same rounding in both of them. This, however, causes an additional numerical problem, because the iterative method diverges when surface currents are added in such small rounded elements. For this reason, surface currents are used to describe only the square (100) and hexagonal (111) facets. This is in practice not a bad approximation, as one needs to somehow introduce a smooth transition between the two different current densities. In terms of setup parameters, a cubic physical domain of side 300 nm was used, surrounded by 300-nm-thick perfectly matched layers. For the finite-element discretization, a mesh of 30,000 domain elements with maximum element size 20 nm and minimum element size 0.5 nm provided converged spectra.

**Funding.** Natur og Univers, Det Frie Forskningsråd (0165-00051B), (7026-00117B); European Research Council (Advanced Grant 789104-eNANO); Ministerio de Economía y Competitividad (MAT2017-88492-R, SEV2015-0522); Centres de Recerca de Catalunya; Fundació Cellex; Villum Fonden (16498); Syddansk Universitet (SDU 2020 funding); Departament d'Empresa i Coneixement, Generalitat de Catalunya.

**Acknowledgment.** J. D. C. is a Sapere Aude research leader supported by Independent Research Fund Denmark. A. R. E. and F. J. G. A. acknowledge support from ERC, the Spanish MINECO, the Catalan CERCA Program, and Fundació Privada Cellex. N. A. M. is a VILLUM Investigator supported by VILLUM FONDEN and Independent Research Fund Denmark. The Center for Nano Optics is financially supported by the University of Southern Denmark. This project has received funding from the Secretaria d'Universitats i Recerca del Departament d'Empresa i Coneixement de la Generalitat de Catalunya, as well as the European Social Fund (L'FSE inverteix en el teu futur)—FEDER. Finite-element calculations were supported by the DeIC National HPC Centre, SDU.

**Disclosures.** The authors declare no conflicts of interest.

**Data Availability.** Data underlying the results presented in this paper are available in Dataset 1, Ref. [78].

**Supplemental document.** See Supplement 1 for supporting content.

## REFERENCES

1. D. K. Gramotnev and S. I. Bozhevolnyi, "Plasmonics beyond the diffraction limit," *Nat. Photonics* **4**, 83–91 (2010).
2. D. K. Gramotnev and S. I. Bozhevolnyi, "Nanofocusing of electromagnetic radiation," *Nat. Photonics* **8**, 13–23 (2014).
3. V. Sandoghdar, "Nano-optics in 2020±20," *Nano Lett.* **20**, 4721–4723 (2020).
4. A. I. Fernández-Domínguez, F. J. García-Vidal, and L. Martín-Moreno, "Unrelenting plasmons," *Nat. Photonics* **11**, 8–10 (2017).
5. S. Lal, S. E. Clare, and N. J. Halas, "Nanoshell-enabled photothermal cancer therapy: impending clinical impact," *Acc. Chem. Res.* **41**, 1842–1851 (2008).
6. A. R. Rastinehad, H. Anastos, E. Wajswol, J. S. Winoker, J. P. Sfakianos, S. K. Doppalapudi, M. R. Carrick, C. J. Knauer, B. Taouli, S. C. Lewis, A. K. Tewari, J. A. Schwartz, S. E. Canfield, A. K. George, J. L. West, and N. J. Halas, "Gold nanoshell-localized photothermal ablation of prostate tumors in a clinical pilot device study," *Proc. Natl. Acad. Sci. USA* **116**, 18590–18596 (2019).
7. P. Wang, B. Huang, Y. Dai, and M.-H. Whangbo, "Plasmonic photocatalysts: harvesting visible light with noble metal nanoparticles," *Phys. Chem. Chem. Phys.* **14**, 9813–9825 (2012).

8. X. Zhang, Y. L. Chen, R.-S. Liu, and D. P. Tsai, "Plasmonic photocatalysis," *Rep. Prog. Phys.* **76**, 046401 (2013).
9. A. Kristensen, J. K. W. Yang, S. I. Bozhevolnyi, S. Link, P. Nordlander, N. J. Halas, and N. A. Mortensen, "Plasmonic colour generation," *Nat. Rev. Mater.* **2**, 16088 (2017).
10. H. A. Atwater and A. Polman, "Plasmonics for improved photovoltaic devices," *Nat. Mater.* **9**, 205–213 (2010).
11. J. G. Smith, J. A. Fauchaux, and P. K. Jain, "Plasmon resonances for solar energy harvesting: a mechanistic outlook," *Nano Today* **10**(1), 67–80 (2015).
12. A. Boltasseva and H. A. Atwater, "Low-loss plasmonic metamaterials," *Science* **331**, 290–291 (2011).
13. I. A. Calafell, J. D. Cox, M. Radonjić, J. R. M. Saavedra, F. J. García de Abajo, L. A. Rozema, and P. Walther, "Quantum computing with graphene plasmons," *npj Quantum Inf.* **5**, 37 (2019).
14. A. I. Fernández-Domínguez, S. I. Bozhevolnyi, and N. A. Mortensen, "Plasmon-enhanced generation of nonclassical light," *ACS Photon.* **5**, 3447–3451 (2018).
15. Z. Zhou, Z. Zhao, Y. Yu, B. Ai, H. Möhwald, R. C. Chiechi, J. K. W. Yang, and G. Zhang, "From 1D to 3D: tunable sub-10 nm gaps in large area devices," *Adv. Mater.* **28**, 2956–2963 (2016).
16. J. J. Baumberg, J. Aizpurua, M. H. Mikkelsen, and D. R. Smith, "Extreme nanophotonics from ultrathin metallic gaps," *Nat. Mater.* **18**, 668–678 (2019).
17. A. Kossov, V. Merk, D. Simakov, K. Leosson, S. Kéna-Cohen, and S. A. Maier, "Optical and structural properties of ultra-thin gold films," *Adv. Opt. Mater.* **3**, 71–77 (2014).
18. R. A. Maniara, D. Rodrigo, R. Yu, J. Canet-Ferrer, D. S. Ghosh, R. Yongsunthon, D. E. Baker, A. Rezikyan, F. J. García de Abajo, and V. Pruneri, "Tunable plasmons in ultrathin metal films," *Nat. Photonics* **13**, 328–333 (2019).
19. Z. M. Abd El-Fattah, V. Mkhitarian, J. Brede, L. Fernández, C. Li, Q. Guo, A. Ghosh, A. Rodríguez Echarri, D. Naveh, F. Xia, J. E. Ortega, and F. J. García de Abajo, "Plasmonics in atomically thin crystalline silver films," *ACS Nano* **13**, 7771–7779 (2019).
20. A. Boltasseva and V. M. Shalaev, "Transdimensional photonics," *ACS Photon.* **6**, 1–3 (2019).
21. P. A. D. Gonçalves, *Plasmonics and Light-Matter Interactions in Two-Dimensional Materials and in Metal Nanostructures: Classical and Quantum Considerations* (Springer Nature, 2020).
22. J.-S. Huang, V. Callegari, P. Geisler, C. Bruening, J. Kern, J. C. Prangma, X. Wu, T. Feichtner, J. Ziegler, P. Weinmann, M. Kamp, A. Forchel, P. Biagioni, U. Sennhauser, and B. Hecht, "Atomically flat single-crystalline gold nanostructures for plasmonic nanocircuitry," *Nat. Commun.* **1**, 150 (2010).
23. B. Hoffmann, M. Y. Bashouti, T. Feichtner, M. Mačković, C. Dieker, A. M. Salaheldin, P. Richter, O. D. Gordan, D. R. T. Zahn, E. Spiecker, and S. Christiansen, "New insights into colloidal gold flakes: structural investigation, micro-ellipsometry and thinning procedure towards ultrathin monocrystalline layers," *Nanoscale* **8**, 4529–4536 (2016).
24. R. Méjard, A. Verdy, O. Demichel, M. Petit, L. Markey, F. Herbst, R. Chassagnon, G. C. des Francs, B. Cluzel, and A. Bouhelier, "Advanced engineering of single-crystal gold nanoantennas," *Opt. Mater. Express* **7**, 1157–1168 (2017).
25. F. Cheng, C.-J. Lee, J. Choi, C.-Y. Wang, Q. Zhang, H. Zhang, S. Gwo, W.-H. Chang, X. Li, and C.-K. Shih, "Epitaxial growth of optically thick, single crystalline silver films for plasmonics," *ACS Appl. Mater. Interfaces* **11**, 3189–3195 (2019).
26. K. M. McPeak, S. V. Jayanti, S. J. P. Kress, S. Meyer, S. Iotti, A. Rossinelli, and D. J. Norris, "Plasmonic films can easily be better: rules and recipes," *ACS Photon.* **2**, 326–333 (2015).
27. J. E. Inglesfield, "Surface electronic structure," *Rep. Prog. Phys.* **45**, 223–284 (1982).
28. W. Shockley, "On the surface states associated with a periodic potential," *Phys. Rev.* **56**, 317–323 (1939).
29. J. M. Pitarke, V. M. Silkin, E. V. Chulkov, and P. M. Echenique, "Theory of surface plasmons and surface plasmon polaritons," *Rep. Prog. Phys.* **70**, 1–87 (2007).
30. P. M. Echenique, J. Osma, M. Machado, V. M. Silkin, E. V. Chulkov, and J. M. Pitarke, "Surface-state electron dynamics in noble metals," *Prog. Surf. Sci.* **67**, 271–283 (2001).
31. S. Suto, K.-D. Tsuei, E. W. Plummer, and E. Burstein, "Surface-plasmon energy and dispersion on Ag single crystals," *Phys. Rev. Lett.* **63**, 2590–2593 (1989).
32. B. Diaconescu, K. Pohl, L. Vattuone, L. Savio, P. Hofmann, V. M. Silkin, J. M. Pitarke, E. V. Chulkov, P. M. Echenique, D. Fariás, and M. Rocca, "Low-energy acoustic plasmons at metal surfaces," *Nature* **448**, 57–59 (2007).
33. A. Politano, V. M. Silkin, I. A. Nechaev, M. S. Vitiello, L. Viti, Z. S. Aliev, M. B. Babanly, G. Chiarello, P. M. Echenique, and E. V. Chulkov, "Interplay of surface and Dirac plasmons in topological insulators: the case of Bi<sub>2</sub>Se<sub>3</sub>," *Phys. Rev. Lett.* **115**, 216802 (2015).
34. A. Varas, P. García-González, J. Feist, F. J. García-Vidal, and A. Rubio, "Quantum plasmonics: from jellium models to ab initio calculations," *Nanophotonics* **5**, 409–426 (2016).
35. W. Zhu, R. Esteban, A. G. Borisov, J. J. Baumberg, P. Nordlander, H. J. Lezec, J. Aizpurua, and K. B. Crozier, "Quantum mechanical effects in plasmonic structures with subnanometre gaps," *Nat. Commun.* **7**, 11495 (2016).
36. P. J. Feibelman, "Surface electromagnetic fields," *Prog. Surf. Sci.* **12**, 287–407 (1982).
37. T. Christensen, W. Yan, A.-P. Jauho, M. Soljačić, and N. A. Mortensen, "Quantum corrections in nanoplasmonics: shape, scale, and material," *Phys. Rev. Lett.* **118**, 157402 (2017).
38. P. A. D. Gonçalves, T. Christensen, N. Rivera, A.-P. Jauho, N. A. Mortensen, and M. Soljačić, "Plasmon-emitter interactions at the nanoscale," *Nat. Commun.* **11**, 366 (2020).
39. A. Liebsch, *Electronic Excitations at Metal Surfaces* (Springer, 1997).
40. P. A. D. Gonçalves, T. Christensen, N. M. R. Peres, A.-P. Jauho, I. Epstein, F. H. L. Koppens, M. Soljačić, and N. A. Mortensen, "Quantum surface-response of metals revealed by acoustic graphene plasmons," *Nat. Commun.* (2021).
41. W. Yan, M. Wubs, and N. A. Mortensen, "Projected dipole model for quantum plasmonics," *Phys. Rev. Lett.* **115**, 137403 (2015).
42. Y. Yang, D. Zhu, W. Yan, A. Agarwal, M. Zheng, J. D. Joannopoulos, P. Lalanne, T. Christensen, K. K. Berggren, and M. Soljačić, "A general theoretical and experimental framework for nanoscale electromagnetism," *Nature* **576**, 248–252 (2019).
43. E. V. Chulkov, V. M. Silkin, and P. M. Echenique, "Image potential states on metal surfaces: binding energies and wave functions," *Surf. Sci.* **437**, 330–352 (1999).
44. A. Rodríguez Echarri, J. D. Cox, and F. J. García de Abajo, "Quantum effects in the acoustic plasmons of atomically-thin heterostructures," *Optica* **6**, 630–641 (2019).
45. A. Liebsch, "Surface-plasmon dispersion and size dependence of Mie resonance: silver versus simple metals," *Phys. Rev. B* **48**, 11317–11328 (1993).
46. A. Liebsch and W. Schaich, "Influence of a polarizable medium on the nonlocal optical response of a metal surface," *Phys. Rev. B* **52**, 14219–14234 (1995).
47. H. B. Michaelson, "The work function of the elements and its periodicity," *J. Appl. Phys.* **48**, 4729–4733 (1977).
48. P. B. Johnson and R. W. Christy, "Optical constants of the noble metals," *Phys. Rev. B* **6**, 4370–4379 (1972).
49. R. H. Ritchie and A. L. Marusak, "The surface plasmon dispersion relation for an electron gas," *Surf. Sci.* **4**, 234–240 (1966).
50. F. J. García de Abajo, "Nonlocal effects in the plasmons of strongly interacting nanoparticles, dimers, and waveguides," *J. Phys. Chem. C* **112**, 17983–17987 (2008).
51. G. W. Ford and W. H. Weber, "Electromagnetic interactions of molecules with metal surfaces," *Phys. Rep.* **113**, 195–287 (1984).
52. M. Rocca, L. Yibing, F. B. de Mongeot, and U. Valbusa, "Surface plasmon dispersion and damping on Ag(111)," *Phys. Rev. B* **52**, 14947–14953 (1995).
53. S. J. Park and R. E. Palmer, "Plasmon dispersion of the Au(111) surface with and without self-assembled monolayers," *Phys. Rev. Lett.* **102**, 216805 (2009).
54. A. Liebsch, "Surface plasmon dispersion of Ag," *Phys. Rev. Lett.* **71**, 145–148 (1993).
55. V. M. Silkin, J. M. Pitarke, E. V. Chulkov, and P. M. Echenique, "Acoustic surface plasmons in the noble metals Cu, Ag, and Au," *Phys. Rev. B* **72**, 115435 (2005).
56. J. M. Pitarke, V. U. Nazarov, V. M. Silkin, E. V. Chulkov, E. Zaremba, and P. M. Echenique, "Theory of acoustic surface plasmons," *Phys. Rev. B* **70**, 205403 (2004).
57. K. Pohl, B. Diaconescu, G. Vercelli, L. Vattuone, V. M. Silkin, E. V. Chulkov, P. M. Echenique, and M. Rocca, "Acoustic surface plasmon on Cu(111)," *Europhys. Lett.* **90**, 57006 (2010).

58. J. Yan, K. W. Jacobsen, and K. S. Thygesen, "Conventional and acoustic surface plasmons on noble metal surfaces: a time-dependent density functional theory study," *Phys. Rev. B* **86**, 241404 (2012).
59. S. J. Park and R. E. Palmer, "Acoustic plasmon on the Au(111) surface," *Phys. Rev. Lett.* **105**, 016801 (2010).
60. L. Vattuone, M. Smerieri, T. Langer, C. Tegenkamp, H. Pfnür, V. M. Silkin, E. V. Chulkov, P. M. Echenique, and M. Rocca, "Correlated motion of electrons on the Au(111) surface: anomalous acoustic surface-plasmon dispersion and single-particle excitations," *Phys. Rev. Lett.* **110**, 127405 (2013).
61. F. Reinert, G. Nicolay, S. Schmidt, D. Ehm, and S. Hüfner, "Direct measurements of the L-gap surface states on the (111) face of noble metals by photoelectron spectroscopy," *Phys. Rev. B* **63**, 115415 (2001).
62. P. A. D. Gonçalves and N. M. R. Peres, *An Introduction to Graphene Plasmonics*, 1st ed. (World Scientific, 2016).
63. A. Principi, E. van Loon, M. Polini, and M. I. Katsnelson, "Confining graphene plasmons to the ultimate limit," *Phys. Rev. B* **98**, 035427 (2018).
64. D. Alcaraz Iranzo, S. Nanot, E. J. C. Dias, I. Epstein, C. Peng, D. K. Efetov, M. B. Lundeberg, R. Parret, J. Osmond, J.-Y. Hong, J. Kong, D. R. Englund, N. M. R. Peres, and F. H. L. Koppens, "Probing the ultimate plasmon confinement limits with a van der Waals heterostructure," *Science* **360**, 291–295 (2018).
65. I.-H. Lee, D. Yoo, P. Avouris, T. Low, and S.-H. Oh, "Graphene acoustic plasmon resonator for ultrasensitive infrared spectroscopy," *Nat. Nanotechnol.* **14**, 313–319 (2019).
66. I. Epstein, D. Alcaraz, Z. Huang, V.-V. Pusapati, J.-P. Hugonin, A. Kumar, X. M. Deputy, T. Khodkov, T. G. Rappoport, J.-Y. Hong, N. M. R. Peres, J. Kong, D. R. Smith, and F. H. L. Koppens, "Far-field excitation of single graphene plasmon cavities with ultracompressed mode volumes," *Science* **368**, 1219–1223 (2020).
67. F. J. García de Abajo, "Graphene plasmonics: challenges and opportunities," *ACS Photon.* **1**, 135–152 (2014).
68. B. Wunsch, T. Stauber, F. Sols, and F. Guinea, "Dynamical polarization of graphene at finite doping," *New J. Phys.* **8**, 318 (2006).
69. E. H. Hwang and S. D. Sarma, "Dielectric function, screening, and plasmons in two-dimensional graphene," *Phys. Rev. B* **75**, 205418 (2007).
70. N. D. Mermin, "Lindhard dielectric function in the relaxation-time approximation," *Phys. Rev. B* **1**, 2362–2363 (1970).
71. V. Myroshnychenko, E. Carbó-Argibay, I. Pastoriza-Santos, J. Pérez-Juste, L. M. Liz-Marzán, and F. J. García de Abajo, "Modeling the optical response of highly faceted metal nanoparticles with a fully 3D boundary element method," *Adv. Mater.* **20**, 4288–4293 (2008).
72. N. A. Mortensen, S. Raza, M. Wubs, T. Sondergaard, and S. I. Bozhevolnyi, "A generalized nonlocal optical response theory for plasmonic nanostructures," *Nat. Commun.* **5**, 3809 (2014).
73. S. Raza, S. I. Bozhevolnyi, M. Wubs, and N. A. Mortensen, "Nonlocal optical response in metallic nanostructures," *J. Phys. Condens. Matter* **27**, 183204 (2015).
74. F. Ouyang, P. E. Batson, and M. Isaacson, "Quantum size effects in the surface-plasmon excitation of small metallic particles by electron-energy-loss spectroscopy," *Phys. Rev. B* **46**, 15421–15425 (1992).
75. J. A. Scholl, A. L. Koh, and J. A. Dionne, "Quantum plasmon resonances of individual metallic nanoparticles," *Nature* **483**, 421–427 (2012).
76. S. Raza, N. Stenger, S. Kadkhodazadeh, S. V. Fischer, N. Kotesha, A.-P. Jauho, A. Burrows, M. Wubs, and N. A. Mortensen, "Blueshift of the surface plasmon resonance in silver nanoparticles studied with EELS," *Nanophotonics* **2**, 131–138 (2013).
77. S. Raza, S. Kadkhodazadeh, T. Christensen, M. Di Vece, M. Wubs, N. A. Mortensen, and N. Stenger, "Multipole plasmons and their disappearance in few-nanometer silver nanoparticles," *Nat. Commun.* **6**, 8788 (2015).
78. A. Rodríguez Echarri, P. A. D. Gonçalves, C. Tserkezis, F. J. García de Abajo, N. A. Mortensen, and J. D. Cox, "Tabulated Feibelman  $d$ -parameters obtained from quantum mechanical optical response simulations of a noble metal surfaces having either (100) and (111) crystallographic orientation," figshare, (2021) <https://doi.org/10.6084/m9.figshare.13772371>.
79. A. García-Lekue, J. M. Pitarke, E. V. Chulkov, A. Liebsch, and P. M. Echenique, "Role of occupied  $d$  bands in the dynamics of excited electrons and holes in Ag," *Phys. Rev. B* **68**, 045103 (2003).
80. S. D. Kevan and R. H. Gaylord, "High-resolution photoemission study of the electronic structure of the noble-metal (111) surfaces," *Phys. Rev. B* **36**, 5809–5818 (1987).
81. R. Paniago, R. Matzdorf, G. Meister, and A. Goldmann, "Temperature dependence of Shockley-type surface energy bands on Cu (111), Ag (111) and Au (111)," *Surf. Sci.* **336**, 113–122 (1995).
82. M. A. Mueller, T. Miller, and T.-C. Chiang, "Determination of the bulk band structure of Ag in Ag/Cu (111) quantum-well systems," *Phys. Rev. B* **41**, 5214–5220 (1990).
83. I. Matsuda, T. Tanikawa, S. Hasegawa, H. W. Yeom, K. Tono, and T. Ohta, "Quantum-well states in ultra-thin metal films on semiconductor surfaces," *e-J. Surf. Sci. Nanotechnol.* **2**, 169–177 (2004).
84. M. Becker, S. Crampin, and R. Berndt, "Theoretical analysis of STM-derived lifetimes of excitations in the Shockley surface-state band of Ag(111)," *Phys. Rev. B* **73**, 081402 (2006).